Neutron imaging: a new possibility for laboratory observation of hydraulic fractures in shale?

S. ROSHANKHAH*, J. P. MARSHALL†, A. TENGATTINI‡§, E. ANDO‡, V. RUBINO†, A. J. ROSAKIS†, G. VIGGIANI‡ and J. E. ANDRADE†

Hydraulic fracturing, the creation of fractures by high-pressure fluid injection into a solid medium, is of interest to enhance the permeability of rocks. This complex three-dimensional hydro-mechanical process, however, has only been studied in the laboratory by boundary measurements or acoustic techniques with low spatio-temporal resolutions until now. In this paper, direct, high spatial resolution, and near real-time visualisation results of hydraulic fracture generation and propagation in prismatic specimens of Marcellus shale rock under in situ conditions (70 MPa, plane strain) are presented. Poly-methyl methacrylate specimens are also tested under the same conditions to highlight the importance of rocks' internal structure on the response of the tested rock. The results reveal a complex interaction among the injected fluid, the pre-existing natural fractures in shale structure, and the hydraulically induced fracture highlighting the governing role of rock fabric even under high stresses. These measurements are possible due to the unique sensitivity of neutrons to water. Besides the intrinsic interest of the results presented, this exploratory investigation highlights the potential of neutron imaging in elucidating the evolution of fluid flow and fluid-driven fractures, as X-rays have done for the evolution of solid structure only. Further, understanding of the mechanics of fracking will lead to development of more accurate hydro-mechanical constitutive models thus enabling the design of field operations with higher efficiencies.

NOTATION

a	notch length (m)
K_I	stress intensity factor (MPa.m$^{0.5}$)
K_{Ic}	Mode-I fracture toughness
P_b	breakdown pressure (MPa)
R	borehole radius (m)
s	geometrical parameter
$\varepsilon_{1,2,3}$	maximum, intermediate, and minimum principal strains
$\sigma_{1,2,3}$	maximum, intermediate, and minimum principal stresses (MPa)
v	Poisson's ratio

INTRODUCTION

Hydraulic fractures (HFs) are encountered in many important geo-energy and geo-environmental applications, from stimulation of unconventional fossil fuel reservoirs (Economides & Nolte, 2000) and deep geothermal reservoirs (Legarth *et al.*, 2005) to geological energy storage (Bauer *et al.*, 2013) and waste disposal (Tsang *et al.*, 2015). Still, there is a lack of understanding of the underlying physics in the interactions between pre-existing natural fractures and HFs through coupling between fractures, rock matrix and the fluid flow. As a result, field operations underutilise about 30% of the targeted subsurface resources (Lecampion & Desroches,

2015). This is due to inability of existing models to predict the complex fluid interaction with heterogeneous, anisotropic, inelastic, permeable rocks, whose rheology is highly non-linear. Most models that are currently used to predict the response of subsurface geomaterials to hydraulic stimulation have been developed for simple materials (e.g. homogeneous, isotropic, linear and elastic), thus they result in large errors.

Research suggests that both boundary conditions and pattern of pre-existing natural fractures influence the response of rocks to hydraulic stimulation (e.g. Warpinski & Teufel, 1987; da Silva & Einstein, 2018). Direct visualisation of the involved multi-physics phenomena in real rocks, under realistic boundary conditions, and with high spatio-temporal resolution can provide us with necessary tools for direct modelling. Experimentally, progress has been made in the past on visualisation of hydraulic fracture (HF) in model materials – that is, poly-methyl methacrylate (PMMA); yet, these materials are homogeneous and impervious, thus their behaviour can be reasonably approximated by linear elastic fracture mechanics (LEFM) coupled with lubrication theory (e.g. Bunger & Detournay, 2008; Bunger *et al.*, 2013; Lecampion *et al.*, 2017). Natural rocks do not fit in these assumptions. Indirect methods, such as acoustic emissions, have been used to infer the geometry of HFs in rocks (e.g. Groenenboom & Fokkema, 1998), but they do not provide information about interactions between the generated HF with the complex network of anisotropies. Moreover, the spatial resolution of these methods is low compared with characteristic length of fractures (wavelength ≫ 100 times fracture width). At the field scale, characteristics of HFs are evaluated by visualising the structure of subsurface rock mass before and after the treatment. For example, microseismic techniques (Juhlin, 1995; Williams-Stroud *et al.*, 2010), radar (Olsson *et al.*, 1992; Day-Lewis *et al.*, 2002), tracer tests (Maloszewski *et al.*, 1999), and active and passive acoustic

emissions (Williams & Johnson, 2004; Meng & De Pater, 2011) are used. The highest spatial resolution among these methods, however, is in the order of a metre, and this cannot capture the fine fabric of the rock mass that governs its global hydro-mechanical behaviour. The frequency and aperture of main joints can be inferred (with low accuracy – Maxwell *et al.*, 2011) also from the wellbore fluid flow rate and pressure data (Nolte, 1991; Dershowitz *et al.*, 1998). In this research study, the process of HF in Marcellus shale is visualised using a high-power flux neutron source (NeXT-Grenoble, 2018 and Tengattini *et al.*, 2017). These results provide a proof-of-concept, reminiscent of the results obtained with X-ray computed tomography (X-ray CT) in soils (Sun *et al.*, 2011; Kawamoto *et al.*, 2018) and rocks (Viggiani *et al.*, 2004; Lenoir *et al.*, 2007; Jia *et al.*, 2014). This method lends itself as a potential high-impact tool to provide quantitative access to important parameters of HF including the fluid front (Frash *et al.*, 2016; Stavropoulou *et al.*, 2018) and fracture propagation path and speed in heterogeneous media.

EXPERIMENTAL SET-UP

For laboratory physical models of HF to be representative of the field condition, specimens with low fracture toughness and permeability must be used or a liquid with a high viscosity must be injected (De Pater *et al.*, 1994). Due to the distinct hydro-mechanical behaviour of natural rocks (e.g. De Pater & Beugelsdijk, 2005; Potluri *et al.*, 2005; Gale *et al.*, 2007; Dahi-Taleghani & Olson, 2011) from that of simple porous samples (plaster or cement paste, e.g. Van Dam *et al.*, 2000), highlighting the fact that the influence of shales heterogeneous and anisotropic structure on its behaviour cannot be ignored, shale samples are directly tested in this study. The results presented in this study are obtained by injecting regular water ($\mu_w = 0.001$ Pa.s) as a proof-of-principle. A higher viscosity liquid will be used in future experiments.

Testing materials and specimen preparation

Prismatic shale and PMMA specimens ($100 \times 100 \times 25$ mm³) are prepared. Testing PMMA as a model material helps to understand the extent of the influence of pre-existing fractures on shale behaviour when compared with that of a simple homogenous medium such as PMMA. Shale's mechanical properties (average) are like those of PMMA

(refer to the Appendix). Another advantage of PMMA as a model material is its optical transparency, which allows visual assessment of the generated HF without using sophisticated techniques. Marcellus shale is a brittle material, and anisotropy exists in both mechanical and hydraulic properties due to the presence of multiple sets of fractures in its internal structure. In this case, three sets of mutually perpendicular fractures are observed. One set is the horizontal/sub-horizontal bedding planes spaced by a couple of millimetres, which are planes of persistent discontinuity. The other two sets are tensile fractures orthogonal to each other and to bedding planes formed due to the applied vertical maximum principal stress in earth's crust. The latter sets repeat in smaller scales in a self-similar (fractal) pattern. In the scale of the laboratory specimens in this study, and with the available spatial resolutions, they are about 2·5 cm apart. Large faces of shale specimens in this study are parallel to the bedding planes. The prismatic shale samples are machined to the above size by a rock coring company. There was no sign of wetness in specimen's individual vacuumed plastic wraps. There was no attempt to completely dry or water saturate the shale specimens in the laboratory before the tests. A hole ($D = 6.4$ mm) is drilled through the specimen thickness at the centre of the large faces using an oil-based coolant. A 1·6 mm long × 0·8 mm wide notch (blunted tip) is manually sawed along the borehole wall throughout the specimen thickness to initiate the HF from there (Fig. 1(a)).

Loading frame and instrumentation

A frame is designed and built to vertically load a prismatic rock specimen and laterally confine it in a rigid aluminium jacket (Fig. 1(a)). The deformation of aluminium plates under induced lateral loading (per elasticity) is over an order of magnitude lower than the aperture of the HF (approximated per LEFM), thus the assumption of close-to-plane strain condition is valid. A high-pressure stainless-steel tube (6·4 mm outer diameter, 3·2 mm inner diameter) is inserted 19 mm through the borehole. An ultra-high-pressure syringe pump ($P_{max} = 89$ MPa) injects water with a constant flow rate into the specimen. The fluid pressure is measured and recorded by the pump's built-in pressure transducer and data-acquisition system. A face-sealing circular O-ring is installed on the internal face of each lateral plate confining

(a)   (b)
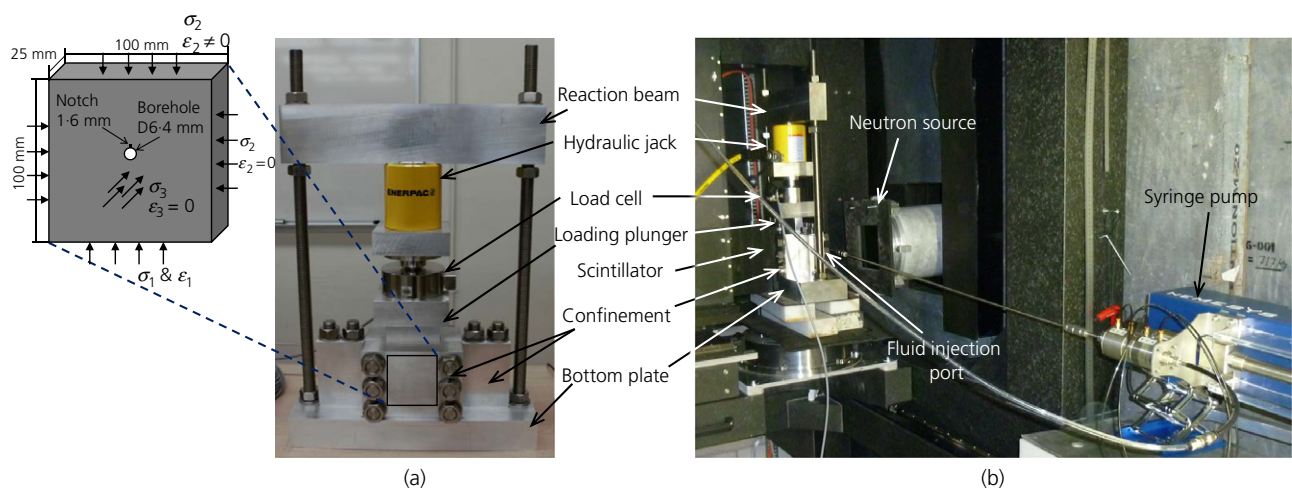
Fig. 1. (a) The loading frame, confining jacket, and schematic view of a prepared specimen with imposed boundary condition (plane strain). (b) Experimental device in the neutron chamber (Institut Laue-Langevin, Grenoble, France). The axis of the neutron beam is perpendicular to the large faces of the loaded specimen. Side view of the loading frame is shown here, and various parts of the set-up are marked

the specimen's large faces to seal the borehole with the aid of silicon-based grease. This configuration also decreases the friction on the large lateral faces. Additionally, contacting surfaces of specimens and confining plates are machined with a mirror finish to decrease the friction between them.

High-resolution process monitoring: neutron imaging
Figure 1(b) shows the experimental device in the neutron imaging chamber. The neutron radiography (two dimensional (2D)) is utilised to monitor the fluid flow in the rock specimen during high-pressure fluid injection, and the neutron tomography (three dimensional (3D)) is utilised to visualise the state of the specimen after the test. Both neutron and X-ray radiations travel through matter and are attenuated according to the well-known Beer–Lambert law. The main difference between them is that for X-rays, attenuation increases with density and atomic number, whereas for neutrons, there is no hard-and-fast rule, but some light elements such as hydrogen and lithium have large attenuation coefficients. Neutrons are suitable, therefore, for detecting water (Perfect *et al*., 2014). There is a further bonus – that is, some materials with good mechanical properties have very low attenuation coefficients, making them ideal pressure vessels. To exploit this fact, confining plates are made of 6061 aluminium alloy in this study. The neutron beam is collimated with a 15 mm pinhole and a 10 m propagation distance to maximise resolution and neutron flux in the testing conditions. Downstream of the experiment, a 100 μm-thick LiF scintillator converts the neutron beam into visible light, which is captured by an s-CMOS camera with 2048×2048 pixels and an exposure time of 700 ms. The radiogram of the specimen on the scintillator is 100×100 mm^2 in size, therefore, the corresponding pixel size in the acquired images is about 50 μm/px. The intensity of the detected full beam (with no sample in place) is used to normalise the beam detected with

the sample in place giving a radiography – that is, field of transmission of the beam through the sample in the direction of the beam. Tomography means acquiring radiographies at many different angles allowing the field of attenuation to be reconstructed in 3D.

## EXPERIMENTAL PROCEDURE AND RESULTS
The experimental procedure and results of tests conducted on four PMMA and four shale specimens are presented here. The testing specimen is first placed in the loading apparatus inside the neutron-imaging chamber. The lateral confinement, vertical loading and the injection equipment are then set. The vertical stress on the specimen is increased gradually until it reaches 70 MPa. Few minutes after that, the syringe pump is turned on. The pump is set to inject regular water at a constant flow rate ($Q = 3$, 6 or 12 ml/min) into the specimen. When the pressure reaches a critical value, fractures form. Figure 2(a) shows the HF created in a PMMA specimen. Pressure histories of four PMMA specimens are presented in Fig. 2(b). The test procedure on shale is the same as PMMAs. Figure 3(a) shows the pressure profiles for tests on shale. The trends look like a typical pressure signature observed in the field (Fig. 3(b)). Figure 4 shows a neutron image of a hydraulically fractured shale specimen initiated from both top and bottom of the wellbore. A video constructed from successive neutron radiographies (Movie S2 online) shows that after a vertical HF forms, it activates a natural fracture. The presence of natural fractures is inferred from the radiographs (Fig. 5(a)). The 3D neutron tomography also shows the bedding planes parallel to large faces (Movie S3 online). A weakened plane parallel to the large faces is observed around the middle of the specimen thickness after the HF, detectable with both the naked eye and neutrons (Fig. 5(b)). The dilated plane is suspected to be the same feature that accumulated water in it after HF occurred (Figs 5(c) and 5(d)).

(a)

(b)
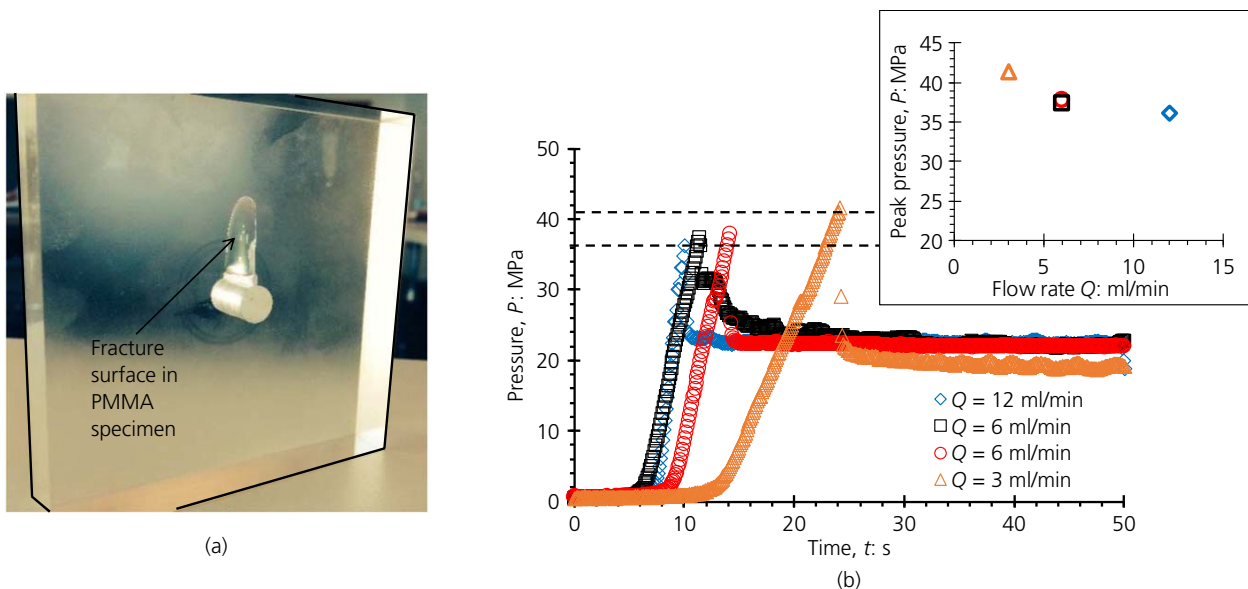
Fig. 2. Results of hydraulic fracturing tests on PMMA. (a) A typical fracture surface in a PMMA specimen. Only one HF is initiated at the tip of the pre-defined notch along the borehole wall at the top, where the maximum tensile stress is concentrated according to elasticity theory, and it propagates vertically upwards in the direction of the maximum compressive stress. The shape of the generated HF is identical in all tests. This image corresponds to $Q = 6$ ml/min. (b) Fluid pressure histories, where a sharp increase in pressure followed by formation of a fracture, a peak pressure near 40 MPa, and a subsequent drop in fluid pressure are recorded. Specimens are fractured hydraulically by injecting regular water at a constant flow rate (3, 6 or 12 ml/min). The measured breakdown pressure (36–41 MPa) is within the predicted range provided by LEFM solutions (refer to the Appendix). The slight variation of breakdown pressure with fluid flow rate (inset graph) may reflect the variation in properties of PMMA specimens
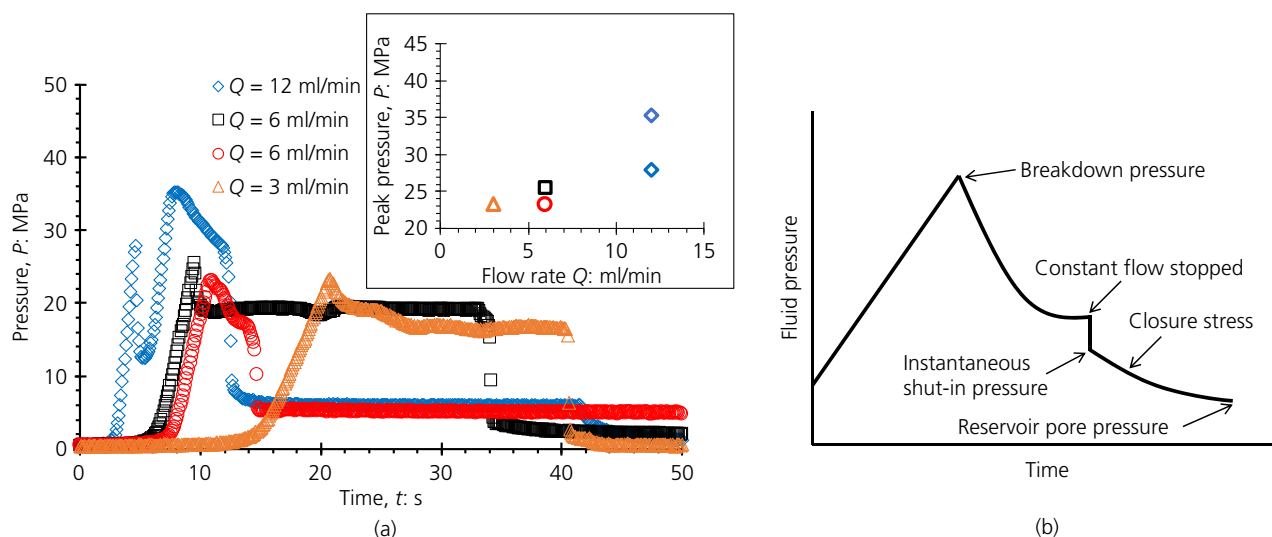
Fig. 3. Results of hydraulic fracturing in shale specimens. (a) Fluid pressure histories for four shale specimens hydraulically fractured by injecting water at a constant flow rate (3, 6 or 12 ml/min). Maximum fluid pressures are measured around 23–35 MPa followed by a clear dropdown. Refer to the Appendix for predicted breakdown pressure for shale per LEFM (7–47 MPa) assuming the bulk, average properties of shale. Given the anisotropic structure of shales, LEFM assumptions are invalid for them, which is evidenced by very different responses obtained for various specimens, even for those fractured with the same flow rates. (b) Typical pressure history observed during hydraulic fracturing operations in the field, with a steady pressure buildup followed by the generation of HFs, maximum pressure (Song *et al*., 2001), a sharp drop in pressure and its transient dissipation (Economides & Nolte, 2000)
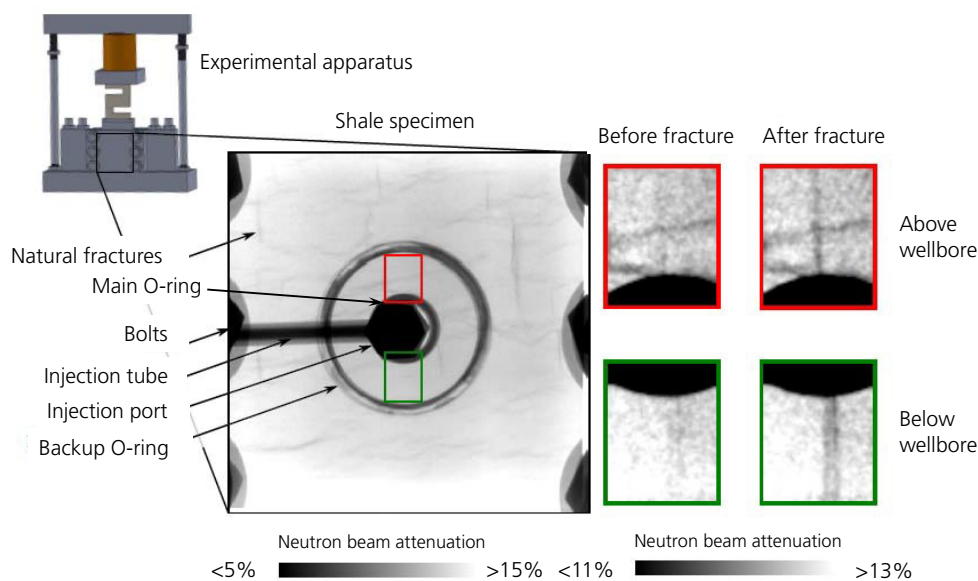

Fig. 4. Typical neutron radiography image of a shale specimen under in situ conditions, and before and after hydraulic fracturing. This image corresponds to the HF generation in shale with flow rate of $Q = 6$ ml/min. The unfractured sample is captured before the peak pressure and the fractured sample is captured immediately after the peak pressure. The time-lapsed images (see Movie S2 online, caption in the Appendix) show two fractures initiated at the top and bottom of the borehole in the direction of the maximum compressive stress (70 MPa). It is interesting to note that the fracture surface bisects the natural fracture present above the borehole (and later it diverts into a bedding plane)

DISCUSSION

The results of this study show several important characteristics about the hydro-mechanical behaviour of natural rocks. The measured maximum pressures for PMMA specimens are close to the breakdown pressure (P_b) predictions derived from LEFM solutions (see the Appendix). The range of breakdown pressure in these calculations is obtained only based on the common range of PMMA's mechanical properties because the fracture propagation regime in this material is toughness dominated, and thus it is mostly independent of the flow rate (Detournay, 2016).

These results show that the high-pressure fluid injection in simple materials produces simple fracture geometry – that is, the fracture initiates from the pre-defined notch at the top of the borehole and propagates with a single plane extended exactly in the expected orientation per imposed boundary conditions (Hubbert & Willis, 1957). In shale specimens, however, the HF is initiated from both top and bottom sides of the wellbore although one notch was fabricated only on top; its orientation is not always exactly vertical (sometimes sub-vertical); and its propagation path deviates from the initial fracture plane (Fig. 5(b) and Movie S2 online).
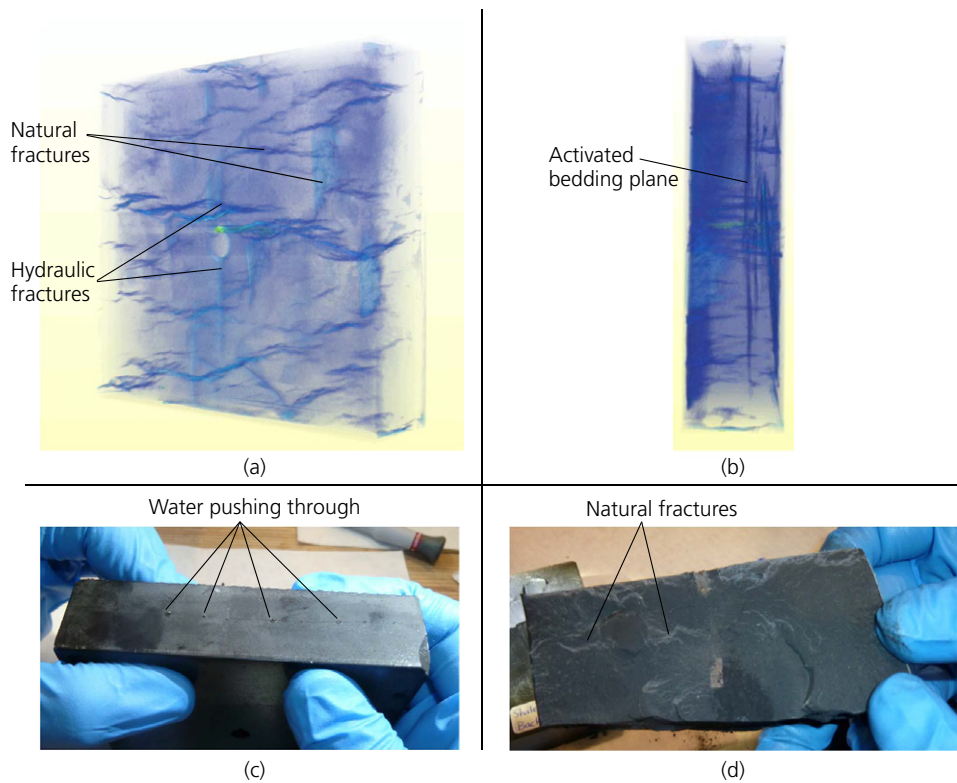
Fig. 5. (a) Neutron radiography of shale specimen after hydraulic fracturing. Image shows rich heterogeneity with an existing natural fracture network. (b) Neutron radiography of shale specimen after hydraulic fracturing from the side. A natural fracture (a bedding plane) is activated following the generation of a HF (with planes perpendicular to one another). Also refer to Movies S1 and S2 online (captions in the Appendix) for neutron radiography and constructed tomography, which show opening of the bedding plane during and after fracturing, respectively. (c) Visual confirmation that the activated natural fracture accumulated water after HF. (d) Visual confirmation of a bedding plane activated due to the HF process. The plane has a rough surface. This plane was closed before formation of the HF; however, an opening, shear slippage, and shear-induced dilation are imposed on it on generation of the HF that significantly increase its fluid conductivity

These observations are attributed to the presence of natural fractures in the shale structure that interact with the HF, redistribute the stresses, interfere with the mechanism of energy dissipation, cause mixed-mode fracturing and propagate in a tortuous path by activating nearby natural fractures. Note that these phenomena govern the behaviour even under very high stresses contrary to the common belief that behaviour of natural geomaterials under high stresses can be estimated with that of simple materials. The governing role of the heterogeneities is also seen in shales' pressure histories – that is, they are neither qualitatively nor quantitatively like those of PMMA although their mechanical properties are close. Specifically, the peak pressure increased with flow rate for shale, while it slightly decreased with flow rate for PMMA. One may think that the porous medium around the borehole fails under a lower pressure when it becomes liquid saturated in shale (Roy *et al.*, 2017), whereas, it is not the case for the impermeable PMMA. Fluid injection with lower flow rate favours a slower pressure rise, the effective stress is redistributed with lower rate, and more fluid leaks off to the surrounding rock, thus a lower breakdown pressure is observed in shale (Zhang & Zhao, 2014). The slight scatter in PMMAs' breakdown pressure P_b, may be simply attributed to the scatter in properties of this synthetic material. The shale specimens do not show the same breakdown pressures even when injected with the same flow rate. The shape of their pressure dissipation responses also differs for all specimens. These show the great variability in geomaterials internal fabric and again the dominance of fabric on their behaviour. Even when the flow rate is increased to 12 ml/min to suppress the influence of

fluid leak-off to the pores and pre-existing fractures so that the energy dissipation occurs mostly through the generation of new surfaces instead of viscous fluid flow (forcing shale to behave more like PMMA), the internal structure of the rock still dominates, and two peaks are recorded in the pressure history. A bedding plane is activated on HF in every shale specimen. Note that natural fractures observed in rock specimens in this study have a rough surface, and they are closed with matched surface asperities and limited liquid conductivity. The significantly increased fluid conductivity of the activated bedding plane (Movie S2 online) (Zimmerman & Bodvarsson, 1996), compared with the rock mass, confirms the induced opening, shear slippage and shear-induced dilation on natural fractures due to the formation of a HF in their vicinity (Rutqvist & Stephansson, 2003; Rutledge *et al.*, 2016). This mechanism is irreversible and generates self-propped fractures that remain productive even after pressure shut-in (e.g. Mayerhofer *et al.*, 1997). In this series of experiments, the crack tip speed is not calculated because it would be consistent with the field conditions only when the fluid viscosity and flow rate are scaled-up. If one assumes the fracture growth rate as small as 1 m/s (Detournay, 2016), to record the position of the crack tip at least at two points x mm apart, one would need to take images with recording rate of $1/x$ fps (frames per second). The current recording rate (1·4 fps) can be improved by about 20 times with the available technology, therefore, achieving 29 fps and capturing the crack tip at two points about 35 mm apart in the next series of these experiments. The complex fracturing process in shale could not have been captured with X-ray radiography (2D), which can only

capture fractures formed normal to the imaging plane. X-ray tomography (3D) would not be fast enough to capture the fracturing process in real time. Neutron radiography, on the contrary, captures the evolution of fluid-filled pores and discontinuities anywhere inside the rock volume during the hydrofracking and projects them on the image's 2D plane, thus one can study the fluid flow and fracture evolution (Stavropoulou *et al.*, 2018).

CONCLUSIONS

In this paper, an experimental set-up is introduced that allows the consistent generation and stable propagation of HFs in natural rocks under high stresses (70 MPa: the stress level at 3 km depth). Water is injected with a constant flow rate to fracture Marcellus shale and PMMA specimens, and their pressure responses are recorded. The flow rate and viscosity of the fracturing liquid are controllable so that, in the future, the process can be scaled to field conditions by injecting more viscous liquids. With this experimental set-up, direct and high-resolution information about the HF geometry and growth rate can be gathered using the neutron-imaging instrument NeXT in Grenoble, France. There are several important points to take away from these results

- Interactions between HFs and pre-existing fractures dominate the hydro-mechanical behaviour of natural rocks, and they are captured within optically opaque specimens using neutrons.
- These results reveal the governing role of rocks internal structure (even under high stresses), which poses significant challenges for numerical models to simulate.
- Integrating observations from the neutron images and data from installed transducers (force, deformation and pressure) will allow quantification of the HF process in natural materials.

ACKNOWLEDGEMENTS

APPENDIX

This section contains calculations to predict breakdown pressure of PMMA and shale specimens per LEFM. Additionally, captions for videos referenced in the main text and presented in the Supplementary Online Materials are presented.

LEFM solution for breakdown pressure

Assuming an elastic, homogeneous, isotropic, impermeable solid under a plane strain condition, one can study the problem of imposed fluid pressure in a circular hole with radius R (m) featuring a vertical notch with length a (m) and aims to determine the breakdown pressure P_b (MPa), the pressure level at which the failure occurs. The geometrical

and loading configuration is shown in Fig. 1(a). The specimen is subject to loading σ_1 (MPa) in the vertical direction, and it is confined laterally in both orthogonal directions. The normal stresses along x_2 and x_3 directions can be expressed as $\sigma_2 = \sigma_3 = \kappa\sigma_1$, where $\kappa = \nu/(1-\nu)$, and ν is Poisson's ratio, by assuming linear elastic constitutive laws and by imposing the boundary conditions $\varepsilon_2 = \varepsilon_3 = 0$. The breakdown pressure is estimated by the following relationship derived from LEFM solutions by computing the stress intensity factor as a function of the pressure and equating it to the fracture toughness, at breakdown. The stress intensity factor K_I (MPa.m$^{0.5}$) is determined using the superposition principle and known solutions to crack problems (Tada *et al.*, 2000; Gdoutos, 2006). The pressure at breakdown is the pressure level attained when the stress intensity factor reaches the fracture toughness K_{Ic} (MPa m$^{0.5}$), and it can be expressed as

$$P_b = \frac{K_{Ic} + \kappa\sigma_1\sqrt{\pi a}\left[(1 - (1/\kappa))F_o^\sigma(s) + (1/\kappa)F_1^\sigma(s)\right]}{\sqrt{\pi a}[(1-\lambda)F_o^P(s) + \lambda F_1^P(s)]}$$

(1)

where s is a geometrical parameter defined as

$$s = \frac{a}{a+R}$$

(2)

where a is the notch length and R the borehole radius. F_1^σ, F_o^σ, F_1^P and F_o^P are following functions of s

$$F_1^\sigma(s) = 2{\cdot}243 - 2{\cdot}64s + 1{\cdot}352s^2 - 0{\cdot}248s^3$$

(3)

$$F_o^\sigma(s) = [1 + 0{\cdot}2(1 - s) + 0{\cdot}3(1 - s)^6]F_1^\sigma(s)$$

(4)

$$F_1^P(s) = 1 + (1 - s)[0{\cdot}5 + 0{\cdot}743(1 - s)^2]$$

(5)

$$F_o^P(s) = [1 + 0{\cdot}2(1 - s) + 0{\cdot}3(1 - s)^6]F_1^P(s)$$

(6)

and λ is a factor ($0 \le \lambda \le 1$) showing that the fluid pressure inside the notch may be less than or equal to the fluid pressure inside the hole. λ is assumed as unity here. The geometric parameters and the vertical stress in experiments conducted in this study are shown in Fig. 1(a), which include $a = 1{\cdot}6$ mm, $R = 3{\cdot}2$ mm and $\sigma_1 = 68$ MPa.

For PMMA. $\nu = 0{\cdot}327$ (Christman, 1972) and K_{Ic} (for quasi-static crack propagation) $= 1{\cdot}05–1{\cdot}55$ MPa.m$^{0.5}$. The lower bound is the average of values measured by several methods as reported by Choi & Salem (1993) and the upper bound is reported by Weerasooriya *et al.* (2006). Also, $K_{Ic} = 3{\cdot}27$ MPa.m$^{0.5}$ is reported by Weerasooriya *et al.* (2006) for dynamic crack propagation. Predicted breakdown pressures for PMMA given the above-mentioned values of ν and K_{Ic} are presented in Table 1. The measured breakdown pressure for all the tested PMMA specimens fall between the predicted pressure for quasi-static fracture propagation (36–41 MPa).

For shale. $\nu = 0{\cdot}15–0{\cdot}4$ (Sone & Zoback, 2013). $K_{Ic} = 0{\cdot}47–0{\cdot}72$ MPa.m$^{0.5}$. The lower bound is reported for Marcellus shale by Lee *et al.* (2015) and the upper bound is reported for Mancos shale by Chandler *et al.* (2016), when the fracture propagates perpendicular to the bedding

Table 1. Fracture toughness and predicted breakdown pressure for PMMA

K_{Ic}: MPa.m$^{0.5}$	1·05	1·55	3·27
P_b: MPa	36	41	56

Table 2. Fracture toughness and predicted breakdown pressure for shale

v	0·15		0·3		0·4	
K_{Ic}: MPa.m$^{0.5}$	0·47	0·72	0·47	0·72	0·47	0·72
P_b: MPa	7·2	9·5	26·5	28·8	44·7	46·9

plane. Predicted breakdown pressures for shale given the above-mentioned values for v and K_{Ic} as well as an average value for $v = 0.3$ are calculated and listed in Table 2.

Note that the measurements (breakdown pressure) and calculations (equation 1) in this study show close mode I fracture toughness values for both PMMA and shale: $K_{Ic} \approx 0.9$ MPa.m$^{0.5}$ (average for shale).

Movie S2

Movie constructed from several successive neutron radiographies showing hydraulic fracturing generation and propagation in a shale specimen. The HF is initiated at both the top and bottom of the wellbore, propagates along the vertical orientation as the imposed boundary conditions require (plane strain), interacts with pre-existing natural fractures, and as a result, activates one of the bedding planes. The movie can be used and distributed if a proper credit is given to its creators; please refer to https://data.caltech.edu/records/1115: 10.22002/D1.1115.

Movie S3

Neutron tomography constructed from neutron radiographies acquired at many different angles showing natural fractures within a shale specimen, the hydraulic fracturing generated from the wellbore along the vertical direction, and the activated bedding plane near the middle of the specimen thickness. The movie can be used and distributed if a proper credit is given to its creators; please refer to https://data.caltech.edu/records/1114: 10.22002/D1.1114.

Pressure data for fractured samples are available at https://doi.org/10.5281/zenodo.825801. Pressure and vertical load histories for shale specimens can be used and distributed if a proper credit is given; please refer to: https://data.caltech.edu/records/1116: 10.22002/D1.1116.

REFERENCES

Bauer, S., Beyer, C., Dethlefsen, F., Dietrich, P., Duttmann, R., Ebert, M., Feeser, V., Goerke, U., Koeber, R., Kolditz, O., Rabbel, W., Schanz, T., Schafer, D., Wuerdemann, H. & Dahmke, A. (2013). Impacts of the use of the geological subsurface for energy storage: an investigation concept. *Environ. Earth Sci.* **70**, No. 8, 3935–3943.

Bunger, A. P. & Detournay, E. (2008). Experimental validation of the tip asymptotics for a fluid-driven crack. *J. Mech. Phys. Solids* **56**, No. 11, 3101–3115.

Bunger, A. P., Gordeliy, E. & Detournay, E. (2013). Comparison between laboratory experiments and coupled simulations of saucer-shaped hydraulic fractures in homogeneous brittle-elastic solids. *J. Mech. Phys. Solids* **61**, No. 7, 1636–1654.

Chandler, M. R., Meredith, P. G., Brantut, N. & Crawford, B. R. (2016). Fracture toughness anisotropy in shale. *J. Geophys. Res.: Solid Earth* **121**, No. 3, 1706–1729.

Choi, S. R. & Salem, J. A. (1993). Fracture-toughness of PMMA as measured with indentation cracks. *J. Mater. Res.* **8**, No. 12, 3210–3217.

Christman, D. R. (1972). *Dynamic properties of poly(methyl methacrylate)*. Washington, DC, USA: Materials and Structures Laboratory, Manufacturing Development, General Motors Corporation, Warren, Michigan, Defense Nuclear Agency.

Dahi-Taleghani, A. & Olson, J. E. (2011). Numerical modeling of multistranded-hydraulic-fracture propagation: accounting for the interaction between induced and natural fractures. *AAPG Bull.* **16**, No. 3, 575–581.

da Silva, B. & Einstein, H. (2018). Physical processes involved in the laboratory hydraulic fracturing of granite: visual observations and interpretation. *Engng Fract. Mech.* **191**, 125–142.

Day-Lewis, F. D., Harris, J. M. & Gorelick, S. M. (2002). Time-lapse inversion of crosswell radar data. *Geophysics* **67**, No. 6, 1740–1752.

De Pater, C. J. & Beugelsdijk, L. J. L. (2005). Experiments and numerical simulation of hydraulic fracturing in naturally fractured rock. *The 40th U.S. symposium on rock mechanics (USRMS), rock mechanics for energy, mineral and infrastructure development in the Northern regions*, pp. 1–12. Anchorage, AK, USA: Alaska rocks, American Rock Mechanics Association.

De Pater, C. J., Cleary, M. P., Quinn, T. S., Barr, D. T., Johnson, D. E. & Weijers, L. (1994). Experimental verification of dimensional analysis for hydraulic fracturing. *SPE Prod. Fac.* **9**, No. 4, 230–238.

Dershowitz, W., La Pointe, P. & Cladouhos, T. (1998). Derivation of fracture spatial pattern parameters from borehole data. *Int. J. Rock Mech. Mining Sci.*, Special issue for 3rd North American rock mechanics symposium, Cancun, Mexico, **35**, No. 4–5, 508.

Detournay, E. (2016). Mechanics of hydraulic fractures. *Annu. Rev. Fluid Mech.* **48**, 311–339.

Economides, M. J. & Nolte, K. G. (2000). *Reservoir stimulation*. New York, NY, USA: Wiley.

Frash, L. P., Carey, J. W. & Viswanathan, H. S. (2016). Notched specimen hydraulic fracturing method for conducting mechanical and hydrological experiments at triaxial reservoir conditions. *Rock mechanics/geomechanics symposium*, Houston, TX, USA: American Rock Mechanics Association.

Gale, J. F. W., Reed, R. M. & Holder, J. (2007). Natural fractures in the Barnett shale and their importance for hydraulic fracture treatments. *AAPG Bull.* **91**, No. 4, 603–622.

Gdoutos, E. E. (2006). *Fracture Mechanics: An Introduction*. Dordrecht, The Netherlands: Springer.

Groenenboom, J. & Fokkema, J. T. (1998). Monitoring the width of hydraulic fractures with acoustic waves. *Geophysics* **63**, No. 1, 139–148.

Hubbert, M. K. & Willis, D. G. (1957). Mechanics of hydraulic fracturing. *Trans. Am. Inst. Mining Metall. Engrs* **210**, No. 6, 153–163.

Jia, L. C., Chen, M. & Jin, Y. (2014). 3D imaging of fractures in carbonate rocks using X-ray computed tomography technology. *Carbonates Evaporites* **29**, No. 2, 147–153.

Juhlin, C. (1995). Imaging of fracture zones in the Finnsjon area, central Sweden, using the seismic reflection method. *Geophysics* **60**, No. 1, 66–75.

Kawamoto, R., Ando, E., Viggiani, G. & Andrade, J. E. (2018). All you need is shape: predicting shear banding in sand with LS-DEM. *J. Mech. Phys. Solids* **111**, 375–392.

Lecampion, B. & Desroches, J. (2015). Simultaneous initiation and growth of multiple radial hydraulic fractures from a horizontal wellbore. *J. Mech. Phys. Solids* **82**, 235–258.

Lecampion, B., Desroches, J., Jeffrey, R. G. & Bunger, A. P. (2017). Experiments versus theory for the initiation and propagation of radial hydraulic fractures in low-permeability materials. *J. Geophys. Res.: Solid Earth* **122**, No. 2, 1239–1263.

Lee, H. P., Olson, J. E., Holder, J., Gale, J. F. W. & Myers, R. D. (2015). The interaction of propagating opening mode fractures with preexisting discontinuities in shale. *J. Geophys. Res.: Solid Earth* **120**, No. 1, 169–181.

Legarth, B., Huenges, E. & Zimmermann, G. (2005). Hydraulic fracturing in a sedimentary geothermal reservoir: results and

implications. *Int. J. Rock Mech. Mining Sci.* **42**, No. 7, 1028–1041.

Lenoir, N., Bornert, M., Desrues, J., Besuelle, P. & Viggiani, G. (2007). Volumetric digital image correlation applied to X-ray microtomography images from triaxial compression tests on argillaceous rock. *Strain* **43**, No. 3, 193–205.

Maloszewski, P., Herrmann, A. & Zuber, A. (1999). Interpretation of tracer tests performed in fractured rock of the Lange Bramke basin, Germany. *Hydrology* **7**, No. 2, 209–218.

Maxwell, S. C., Pope, T., Cipolla, C., Mack, M., Trimbitasu, L., Norton, M. & Leonard, J. (2011). Understanding hydraulic fracture variability through integrating microseismicity and seismic reservoir characterization. *SPE/EAGE European unconventional resources conference & exhibition – from potential to production*, Vienna, Austria, SPE 144207, pp. 482–490. Vienna, Austria: Americas Unconventional Gas.

Mayerhofer, M. J., Richardson, M. F., Walker, R. N., Meehan, D. N., Oehler, M. W. & Browning, R. R. (1997). Proppants? We don't need no proppants. *SPE-38611-MS, SPE Annual technical conference and exhibition*, San Antonio, Texas, pp. 457–464. Society of Petroleum Engineers.

Meng, C. & De Pater, C. J. (2011). Acoustic monitoring of hydraulic fracture propagation in pre-fractured natural rocks. *Key Engng Mater.* **452–453**, 833–836.

NeXT-Grenoble (2018) https://next-grenoble.fr/ (accessed 07/12/2018).

Nolte, K. G. (1991). Fracturing-pressure analysis for nonideal behavior. *J. Petrol. Technol.* **43**, No. 2, 210–218.

Olsson, O., Falk, L., Forslund, O., Lundmark, L. & Sandberg, E. (1992). Borehole radar applied to the characterization of hydraulically conductive fracture zones in crystalline rock. *Geophys. Prospect.* **40**, No. 2, 109–142.

Perfect, E., Cheng, C. L., Kang, M., Bilheux, H. Z., Lamanna, J. M., Gragg, M. J. & Wright, D. M. (2014). Neutron imaging of hydrogen-rich fluids in geomaterials and engineered porous media: a review. *Earth-Sci. Rev.* **129**, 120–135.

Potluri, N. K., Zhu, D. & Hill, A. D. (2005). The effect of natural fractures on hydraulic fracture propagation. *SPE European formation damage conference*, Sheveningen, The Netherlands: Society of Petroleum Engineers, pp. 1–6.

Roy, D. G., Singh, T. N., Kodikara, J. & Das, R. (2017). Effect of water saturation on the fracture and mechanical properties of sedimentary rocks. *J. Geophys. Res.: Solid Earth* **50**, No. 10, 2585–2600.

Rutledge, J., Weng, X., Yu, X., Chapman, C. & Leaney, S. (2016). Bedding-plane slip as a microseismic source during hydraulic fracturing. 86th Annual Meeting of the Society of Exploration Geophysicists. *Technical Program Expanded Abstracts*, Dallas, TX, USA.

Rutqvist, J. & Stephansson, O. (2003). The role of hydromechanical coupling in fractured rock engineering. *Hydrogeol. J.* **11**, No. 1, 7–40.

Sone, H. & Zoback, M. D. (2013). Mechanical properties of shale-gas reservoir rocks, part 1: static and dynamic elastic properties and anisotropy. *Geophysics* **78**, No. 5, 381–392.

Song, I., Suh, M., Won, K. S. & Haimson, B. (2001). A laboratory study of hydraulic fracturing breakdown pressure in tablerock sandstone. *Geosci. J.* **5**, No. 3, 263.

Stavropoulou, E., Andò, E., Tengattini, A., Briffaut, M., Dufour, F., Atkins, D. & Armand, G. (2018). Liquid water uptake in unconfined Callovo Oxfordian clay-rock studied with neutron and X-ray imaging. *Acta Geotech.* 1–15.

Sun, W., Andrade, J. E., Rudnicki, J. W. & Eichhubl, P. (2011). Connecting microstructural attributes and permeability from 3D tomographic images of in situ shear-enhanced compaction bands using multiscale computations. *Geophys. Res. Lett.* **38**, No. 10, L10302.

Tada, H., Paris, P. C. & Irwin, G. R. (2000). *The Stress Analysis of Cracks Handbook*. New York, NY, USA: ASME Press.

Tengattini, A., Atkins, D., Giroud, B., Andò, E., Beaucour, J. & Viggiani, G. (2017). NeXT-Grenoble, a novel facility for neutron and X-ray tomography in Grenoble. *Proceedings of the 3rd international conference on tomography of materials and structures*, Lund, Sweden.

Tsang, C. F., Neretnieks, I. & Tsang, Y. (2015). Hydrologic issues associated with nuclear waste repositories. *Environ. Earth Sci.* **51**, No. 9, 6923–6972.

Van Dam, D. B., De Pater, C. J. & Romijn, R. (2000). Analysis of hydraulic fracture closure in laboratory experiments. *SPE Prod. Fac.* **15**, No. 3, 151–158.

Viggiani, G., Lenoir, N., Besuelle, P., Di Michiel, M., Marello, S., Desrues, J. & Kretzschmer, M. (2004). X-ray microtomography for studying localized deformation in fine-grained geomaterials under triaxial compression. *Comptes Rendus Mec.* **332**, No. 10, 819–826.

Warpinski, N. R. & Teufel, L. W. (1987). Influence of geologic discontinuities on hydraulic fracture propagation. *J. Petrol. Technol.* **39**, No. 2, 209–220.

Weerasooriya, T., Moy, P., Casem, D., Cheng, M. & Chen, W. (2006). Fracture toughness of PMMA as a function of loading rate. *SEM annual conference & exposition on experimental and applied mechanics*, Saint Louis, MO, USA.

Williams, J. H. & Johnson, C. D. (2004). Acoustic and optical borehole-wall imaging for fractured-rock aquifer studies. *J. Appl. Geophys.* **55**, No. 1–2, 151–159.

Williams-Stroud, S., Kilpatrick, J., Cornette, B., Eisner, L. & Hall, M. (2010). Moving outside of the borehole: characterizing natural fractures through microseismic monitoring. *First Break, European Association of Geoscientists & Engineers (EAGE)* **28**, No. 7, 89–94.

Zhang, Q. B. & Zhao, J. (2014). A review of dynamic experimental techniques and mechanical behaviour of rock materials. *Rock Mech. Rock Engng* **47**, No. 4, 1411–1478.

Zimmerman, R. W. & Bodvarsson, G. S. (1996). Hydraulic conductivity of rock fractures. *Transport Porous Media* **23**, No. 1, 1–30.

HOW CAN YOU CONTRIBUTE?

To discuss this paper, please submit up to 500 words to the editor at journals@ice.org.uk. Your contribution will be forwarded to the author(s) for a reply and, if considered appropriate by the editorial board, it will be published as a discussion in a future issue of the journal.